

# Niobium nitride thin films prepared by atomic layer deposition for efficient superconducting nanowire single-photon detectors

Risheng Cheng, Sihao Wang, and Hong X. Tang\*

Department of Electrical Engineering, Yale University, New Haven, CT 06511, USA

(Dated: October 17, 2019)

High-quality ultra-thin films of niobium nitride (NbN) are developed by plasma-enhanced atomic layer deposition (PEALD) technique. Superconducting nanowire single-photon detectors (SNSPDs) patterned from this material exhibit high switching currents and saturated internal efficiencies over a broad bias range at 1550 nm telecommunication wavelength. Statistical analyses on hundreds of fabricated devices show near-unity fabrication yield due to exceptional homogeneity of the films with few defects. This ALD-NbN material is an ideal superconducting material for fabricating large single-photon detector arrays combining high efficiency, low jitter, low dark counts as well as large detection area.

## I. INTRODUCTION

Superconducting nanowire single-photon detectors (SNSPDs)[1] have drawn great attention since their first implementation[2] due to their excellent performances, including high efficiency[3–6], fast speed[7, 8], low timing jitter[9–11] and ultra-low dark count rates[12, 13]. In addition, their suitability of on-chip integration with various nanophotonics circuits [14–25] as well as their photon number[26–28] and spectral resolving capability[29–31] render them a very promising technology for the applications in quantum optics, quantum communications and quantum information processing[32–34].

The SNSPD is typically a narrow nanowire (20 nm - 150 nm width) patterned from an ultra-thin superconducting film (3-10 nm thickness) for efficient visible and telecom photon detection. So far, there are two main classes of superconducting materials developed and made into high-efficiency SNSPDs: (1) poly-crystalline nitride superconductors such as NbN[4, 15, 35] and NbTiN[5, 16, 36–38]; (2) amorphous alloy superconductors, such as WSi[3, 39], MoSi[6, 11, 22, 40, 41] and MoGe[42]. In comparison with conventional Nb(Ti)N, the latter amorphous materials have smaller superconducting energy gap and lower electron density, which tend to create larger photon-excited hot spots in the nanowires and lead to better saturated internal efficiency. The structural homogeneity due to the absence of grain boundaries in the amorphous films enable the fabrication of large-area detector arrays without suffering severely from constriction[43, 44]. The drawback is their relatively lower superconducting transition temperature  $T_c$  ( $< 5$  K for thin films) which sets the operation temperature of the amorphous detectors below 2.5 K for saturated efficiency at 1550 nm wavelength[45]. Nb(Ti)N-based detectors, on the other hand, have higher  $T_c$ , higher critical current, relatively improved jitter performance and more immunity to latching at high operation speed due to their shorter hot spot relaxation time[46–48]. Consequently, Nb(Ti)N was exploited in the recent demonstration of GHz-counting-rate detectors[7, 8] and sub-3 ps timing jitter[9].

In this Article, we show our development of high-quality NbN thin films by plasma-enhanced atomic layer deposition

(PEALD) and their applications in SNSPDs fabrication. The fabricated detectors demonstrate broad saturated plateaus in the efficiency curves that are comparable with amorphous detectors and without compromising high switching currents. Statistical measurement over hundreds of detectors show a close-to-unity fabrication yield of large-area detectors and thus indicate the ultra-high homogeneity of our films, which provides basis for realizing large array of single-photon detectors with saturated efficiency and low timing jitter.

## II. FILM PREPARATION

The NbN films are prepared by the Ultratech/CNT Fiji ALD system using (tert-butylimido)-tris(diethylamido)-niobium(V) (TBTDEN) as the niobium precursor and mixed  $N_2/H_2$  as the plasma gas. In each cycle of deposition, the substrate is first exposed to the precursor to form a monolayer of TBTDEN on the surface, which is later reduced to NbN by reacting with the plasma. Ar purging is performed prior to each plasma step for removing residual TBTDEN. By alternately repeating these steps, the NbN film is deposited on the substrate with atomic level thickness control. The best results combining the highest  $T_c$  as well as the lowest resistivity are achieved at the substrate temperature of 300 °C and 300 W plasma power. More details on the preparation process including other optimized parameters could be found in Ref.[49].

Figure 1(a) plots the measured thickness of the NbN films deposited with varying cycle numbers. All the NbN films are deposited on thermally oxidized Si chips with 330 nm-thick LPCVD-grown  $SiN_x$  on top for the future integration of the SNSPDs with photonic circuits[16, 30]. The thickness is measured by a spectroscopic ellipsometer (J.A. Woolam M-2000). The slope extracted from the linear fit (dashed line) indicates a deposition rate  $DR = 0.68 \pm 0.01 \text{ \AA/cycle}$ . Figure 1(b) shows the sheet resistance measured by the four probe and van der Pauw method on the unpatterned bare NbN films as a function of the cycle number. The dashed line represents a fit to the experimental data using the equation  $R_{\text{sheet}} = B/(x - a)$ , where  $R_{\text{sheet}}$  and  $x$  denote the sheet resistance and the cycle number, respectively. The best fitting is done by the set of free parameters  $B = 38178 \Omega/\text{sq}$  and  $a = 52.9$ . The non-zero value of  $a$  suggests the existence of “dead cycles”, which does not contribute to the conductance of the film. Based on the obtained  $DR$  in Fig. 1(a), we esti-

\* hong.tang@yale.edu

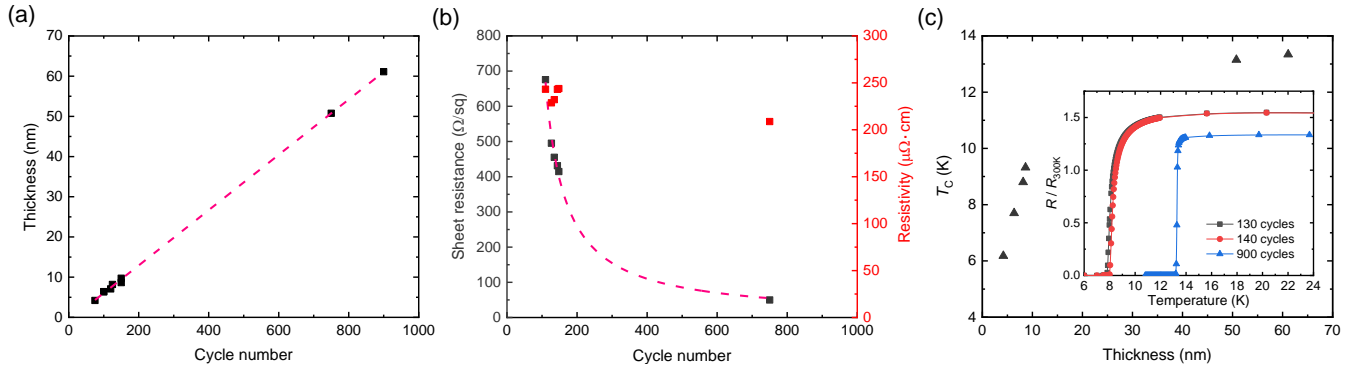


FIG. 1. (a) Measured NbN film thickness versus the ALD cycle number. The dashed line is a linear fit, whose slope indicates the deposition rate of  $0.68 \text{ \AA}/\text{cycle}$ . (b) Measured sheet resistance ( $R_{\text{sheet}}$ ) and calculated resistivity of the NbN films versus the ALD cycle number ( $x$ ). The dashed line represents a fit by the equation  $R_{\text{sheet}} = B/(x-a)$  with  $B$  and  $a$  as free fitting parameters. (c)  $T_c$  of the NbN films versus the thickness. Inset: resistance of three NbN films versus temperature showing the superconducting transition. The resistance is normalized by the room temperature value  $R_{300\text{K}}$ .

mate the corresponding thickness to the “dead cycles” to be  $3.6 \text{ nm}$ , which is significantly larger than the sputtered NbN films shown in other work[50], and the underlying mechanism is subject to further investigation. We also demonstrate in Fig.1 (b) the calculated resistivity by multiplying  $R_{\text{sheet}}$  with the effective thickness  $(x-a) \times DR$ . We observe consistent results around  $240 \mu\Omega \cdot \text{cm}$  for the thin films ( $<10 \text{ nm}$  thickness), which is slightly larger than  $210 \mu\Omega \cdot \text{cm}$  obtained from the relatively thick film ( $>50 \text{ nm}$  thickness).

In order to investigate the superconducting property of the NbN films, multiple NbN chips are cooled down in a physical property measurement system (Quantum Design PPMS Dyna-Cool) to record the temperature dependence of the resistance. Figure 2(c) shows the  $T_c$  versus the thickness of the NbN films, which is defined as the temperature where the resistance of the film is dropped to 50% of  $R_{20\text{K}}$  the resistance measured at 20 K. As expected, higher  $T_c$  is observed for thicker film, and it tends to saturate at  $13.3 \text{ K}$  with  $61 \text{ nm}$  thickness (900 cycles). The inset of Fig. 2(c) shows the zoomed-in view of the resistance versus temperature curves around the superconducting transition region. The very sharp transition shown by the 900-cycles film with only  $0.15 \text{ K}$  transition width (90% to 10% of  $R_{20\text{K}}$ ) suggests high homogeneity and uniformity of the deposited film. The 130-cycles and 140-cycles films that are later fabricated into nanowire detectors have reduced  $T_c$  around  $8 \text{ K}$  and broader transition with  $1.7 \text{ K}$  width.

### III. DEVICE FABRICATION

We fabricate SNSPDs by patterning the 130-cycles and 140-cycles NbN films deposited on  $\text{SiN}_x$  chips. We define superconducting nanowires by the exposure of negative-tone 6% hydrogen silsesquioxane (HSQ) resist using high-resolution (100kV) electron-beam lithography (Raith EBPG5200) and the subsequent development in tetramethylammonium hydroxide (TMAH)-based developer MF-312. In a second electron-beam lithography step, electrode pads are defined using double-layer polymethyl methacrylate (PMMA) positive-tone resist. After the development in the mixture of methyl

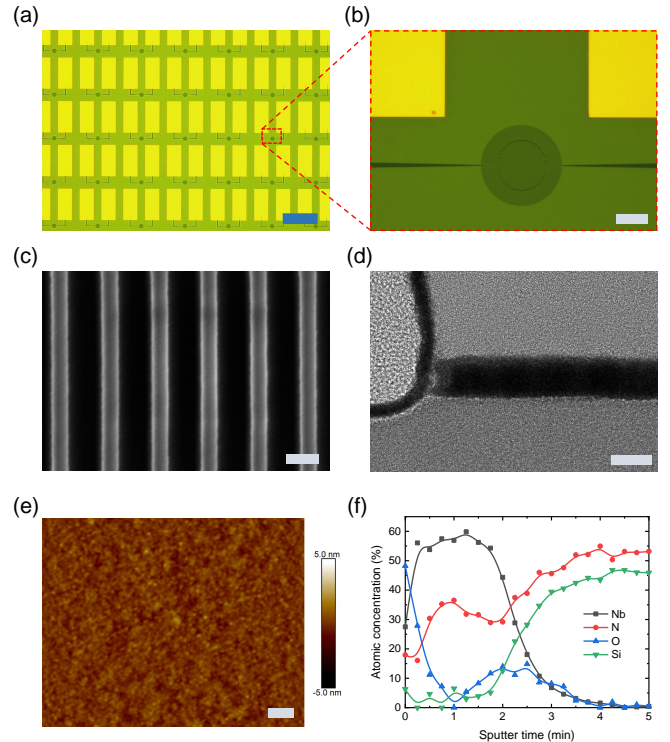


FIG. 2. (a) Optical micrograph of fabricated SNSPD array. Scale bar,  $200 \mu\text{m}$ . (b) Close-up view of the nanowire detection area of an SNSPD. Scale bar,  $10 \mu\text{m}$ . (c) Close-up SEM image of an SNSPD with  $50 \text{ nm}$ -width nanowires. The pitch of the nanowires are kept three times of the width. Scale bar,  $100 \text{ nm}$ . (d) TEM image taken at the edge of the nanowire cross-section patterned from the 140-cycles NbN film. The HSQ mask is left on top after fabrication. Scale bar,  $10 \text{ nm}$ . (e) AFM image taken on the bare 140-cycles NbN film prior to the device patterning. Scale bar,  $100 \text{ nm}$ . (f) XPS measurement results of the 140-cycles NbN film showing the depth profile of the atomic concentration for multiple concerned elements.

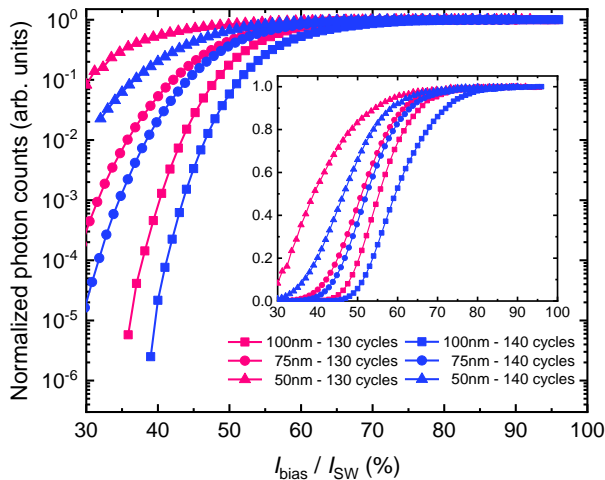


FIG. 3. Normalized photon counts versus the relative bias current ( $I_{\text{bias}}/I_{\text{SW}}$ ) for SNSPDs of varying width and thickness. Inset: linear plots of the normalized photon counts used to define the saturation current  $I_{\text{sat}}$ .

isobutyl ketone (MIBK) and isopropyl alcohol (IPA), we liftoff electron-beam evapoated 10 nm-thick Cr adhesion layer and 100 nm-thick Au in acetone to form the contact pads. Later, the HSQ nanowire pattern is transferred to the NbN layer in a timed reactive-ion etching (RIE) step employing tetrafluoromethane ( $\text{CF}_4$ ) chemistry.

On each NbN chip, we fabricate a total of 450 SNSPDs with three different designs that respectively employ nanowires of 50 nm, 75 nm and 100 nm nominal width (Fig. 2(a)). As shown in Fig. 2(b), the nanowires are meandered into a circular shape with 15  $\mu\text{m}$  diameter to form the active detection area, while the pitch of the nanowires are kept three times of the width. The extra floating nanowires surrounding the active area are for proximity effect correction during the electron-beam exposure, which constitute a larger circle of 25  $\mu\text{m}$  diameter along with the active area. Figure 2(c) shows the scanning electron micrograph (SEM) image for one of the 50 nm-width devices. The fabricated nanowires demonstrate high uniformity with the variation of the nanowire width less than 5 nm across the whole active area of the device. In the meantime, the uniformity of the long nanowires are also guaranteed by the ultra-smooth surface of the NbN film. As visualized in Fig. 2(e), the atomic force micrograph (AFM) image taken on the NbN film prior to the device patterning demonstrate a better than 0.4 nm root-mean-square surface roughness with negligible difference from the original  $\text{SiN}_x$  substrate.

Figure 2(d) presents the transmission electron micrograph (TEM) image taken at the edge of the nanowire cross-section with the HSQ mask left on top. The total thickness of the nanowire (patterned from 140-cycles NbN film) is approximately 9.5 nm including the 2 nm-thick native oxide layer, which could be distinguished from slight color difference. For further investigation of the elemental composition, we perform X-ray photoelectron spectroscopy (XPS) measurement on the unpatterned NbN film. By slowly sputtering the tar-

get film using focused Ar ion beam, the depth profile of the atomic concentration for multiple concerned elements could be obtained, as shown in Fig. 2(f). The existence of the native oxide layer is further confirmed by the high concentration of oxygen observed during the first 0.5 minute sputtering, which decays rapidly as the element analysis is performed deeper into the film. Notably, we observe another oxygen peak at the interface between NbN and  $\text{SiN}_x$  substrate. The existence of this initial layer of oxide leads to change in the property of NbN films and could be the origin of the aforementioned “dead cycles”. A separate XPS measurement is also carried out on the thicker 900-cycles NbN film after 6 minutes Ar sputtering to completely remove the surface oxide layer and any potential contamination of the film. The element analysis results indicate 60-65% concentration of Nb and 35-40% N with negligible presence of other elements.

#### IV. DEVICE CHARACTERIZATION

The detector chips are mounted on a 3-axis stack of Attocube stages inside a closed-cycle refrigerator and cooled down to 1.7 K base temperature. In order to characterize the optical response of the fabricated detectors, 1550 nm continuous wave (CW) laser light is attenuated to the single-photon level and sent to the detector chips via a standard telecommunication fiber (SMF-28) installed in the refrigerator. The detectors are flood-illuminated by fixing the fiber tip far away from the surface of the detector chips, and the diameter of the provided beam spot on the chip is estimated to be around 2 mm. We control the Attocube stages by the LabVIEW program to move the detector chips and make the electrical contact between the RF probes and the gold pads of the detectors. The RF probes are connected to a coaxial cable installed in the refrigerator, and the room-temperature end of the cable is attached to a bias-tee (Mini-Circuits ZFBT-6GW+) to separate the DC bias current and RF output pulses for the detectors. The output pulses are amplified by a low-noise RF amplifier (RF bay LNA-650) and sent to a fast oscilloscope for pulse observation or a pulse counter (PicoQuant PicoHarp 300) for the photon counting measurement.

All the detectors are screened by an automated measurement program, and several best detectors with the highest switching currents  $I_{\text{SW}}$  are selected for subsequent more detailed optical characterization. Figure 3 plots the normalized photon counts as a function of the relative bias current ( $I_{\text{bias}}/I_{\text{SW}}$ ) for SNSPDs of different width and thickness. The  $I_{\text{SW}}$  of the 100 nm, 75 nm and 50 nm-width nanowires patterned from the 140-cycles (130-cycles) NbN film are 21.9  $\mu\text{A}$  (17.6  $\mu\text{A}$ ), 16.3  $\mu\text{A}$  (12.4  $\mu\text{A}$ ) and 11.1  $\mu\text{A}$  (6.9  $\mu\text{A}$ ), respectively. All the measured detectors demonstrate very broad saturated response plateaus, indicating near-unity internal efficiencies of the detectors. The broad plateaus not only render the detectors less sensitive to the constriction but also enable the operation of the detectors at lower bias region with much lower intrinsic dark counts and without compromising high efficiency. It is also worth noting that the similar broad plateaus have only been shown in amorphous detectors[3] or sputtered NbN detectors made of ultra-narrow nanowires with reduced switching currents[51]. In comparison, our 100 nm-

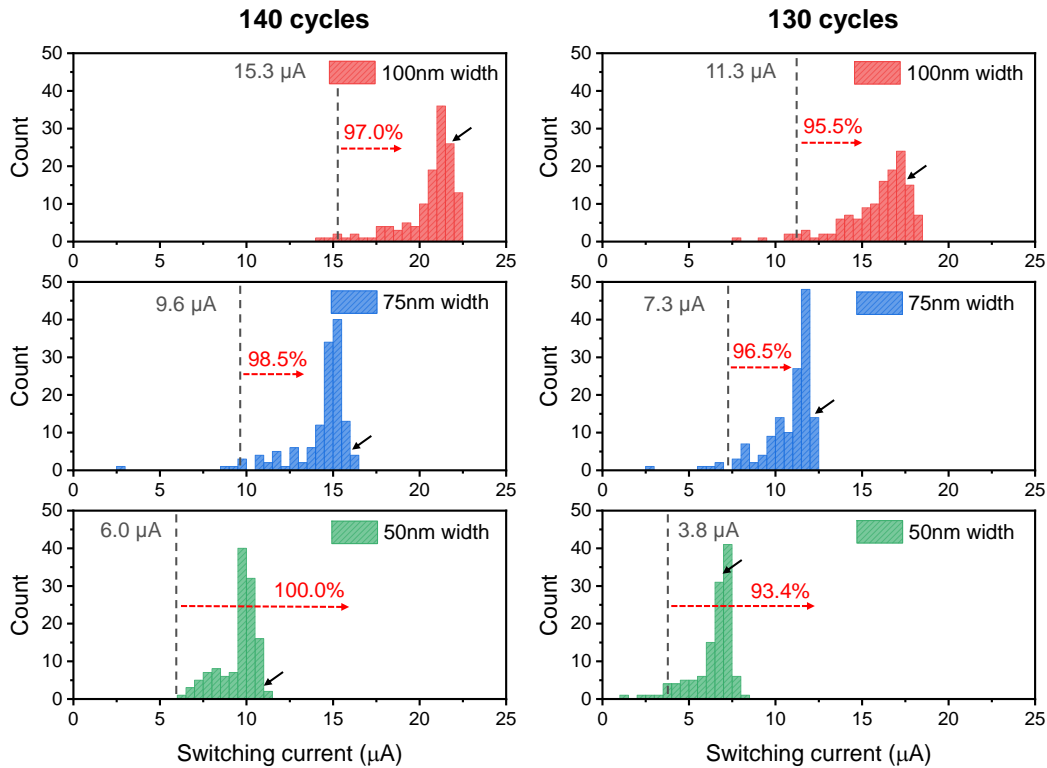


FIG. 4. Histogram of  $I_{SW}$  measured for SNSPDs of varying width and thickness. The gray dashed lines represent  $I_{sat}$  for each types of devices, and the calculated fabrication yields are shown on the red dashed arrows.  $I_{SW}$  of the reference detectors shown in Fig. 3 are marked using the black solid arrows.

width detectors still demonstrate a well-saturated efficiency with a significantly improved switching current larger than  $20\ \mu\text{A}$ , which eases the fabrication process and also show great promise for realizing faster detectors with low timing jitter.

The high homogeneity of our NbN films could also be seen in the  $I_{SW}$  histogram for the detectors of different design visualized in Fig. 4. The results show highly concentrated distribution of  $I_{SW}$  with just a small number of nanowires showing reduced  $I_{SW}$  due to the constriction. Since it is extremely time-consuming to perform the optical characterization for all the detectors, we compare the  $I_{SW}$  with the reference detectors of the same design shown in Fig. 3 for the estimation of the fabrication yield. For each type of detectors, we define the saturation current  $I_{sat}$  as the current where 90% of the maximum counting rates is reached and labeled them in gray dashed lines in Fig. 4. The fabrication yield is calculated as the ratio of the number of the detectors with  $I_{SW} > I_{sat}$  to the total number. Despite the large areas of the detectors, fabrication yields exceeding 93% are recorded for all types of detectors. In particular, a 100% yield is demonstrated with 50 nm-width detectors patterned from the 140-cycles NbN film due to the broader saturation plateau with narrower width and better uniformity in thickness compared to the slightly thinner 130-cycles film.

## V. CONCLUSION

Based on PEALD technique, we have prepared high quality, uniform NbN films with  $T_c$  of up to 13.3 K and atomic level thickness control. The SNSPDs made from this material simultaneously demonstrate broad saturated efficiency plateaus and high  $I_{SW}$  larger than  $20\ \mu\text{A}$ . These features not only allow for the operation of the detectors at lower dark counts regime without compromising high efficiencies and low jitters but also render the detectors less sensitive to the constriction when fabricating large-area detector arrays. In addition, the statistical analysis on the  $I_{SW}$  histogram measured for hundreds of detectors show a strikingly high fabrication yield approaching unity, which we attribute to the exceptional homogeneity of the film with very few defects.

We expect a detector system with  $>90\%$  efficiency is achievable by integrating the ALD-NbN detector with an optical cavity in the near future[3–6]. We also envision the ALD-NbN material will play an important role in the fabrication of integrated quantum photonic circuits where on-chip waveguide-integrated SNSPDs are in great demand.

During the preparation of this manuscript, we became aware of the work by Knehr et al. on SNSPDs made from ALD-NbN [52].

## ACKNOWLEDGMENTS

We acknowledge funding support from DARPA DETECT program through an ARO grant (No: W911NF-16-2-0151),

NSF EFRI grant (EFMA-1640959), AFOSR MURI grant (FA95550-15-1-0029), and the Packard Foundation. The authors would like to thank Michael Power, Sean Rinehart, Kelly Woods, Dr. Yong Sun, Dr. Min Li, Dr. Lei Wang and Dr. Michael Rooks for their assistance provided in the film deposition, characterization and device fabrication. The characterization of the NbN films was done at the Yale West Campus Materials Characterization Core (MCC). The fabrication of the devices was done at the Yale School of Engineering & Applied Science (SEAS) Cleanroom and the Yale Institute for Nanoscience and Quantum Engineering (YINQE).

## REFERENCES

- [1] C. M. Natarajan, M. G. Tanner, and R. H. Hadfield, *Superconductor Science and Technology* **25**, 063001 (2012).
- [2] G. Gol'tsman, O. Okunev, G. Chulkova, A. Lipatov, A. Semenov, K. Smirnov, B. Voronov, A. Dzardanov, C. Williams, and R. Sobolewski, *Applied Physics Letters* **79**, 705 (2001).
- [3] F. Marsili, V. B. Verma, J. A. Stern, S. Harrington, A. E. Lita, T. Gerrits, I. Vayshenker, B. Baek, M. D. Shaw, R. P. Mirin, *et al.*, *Nature Photonics* **7**, 210 (2013).
- [4] W. Zhang, L. You, H. Li, J. Huang, C. Lv, L. Zhang, X. Liu, J. Wu, Z. Wang, and X. Xie, *Science China Physics, Mechanics & Astronomy* **60**, 120314 (2017).
- [5] I. Esmaeil Zadeh, J. W. Los, R. B. Gourgues, V. Steinmetz, G. Bulgarini, S. M. Dobrovolskiy, V. Zwiller, and S. N. Dorenbos, *APL Photonics* **2**, 111301 (2017).
- [6] D. V. Reddy, R. R. Nerem, A. E. Lita, S. W. Nam, R. P. Mirin, and V. B. Verma, in *CLEO: QELS Fundamental Science* (Optical Society of America, 2019) pp. FF1A–3.
- [7] W. Zhang, J. Huang, C. Zhang, L. You, C. Lv, L. Zhang, H. Li, Z. Wang, and X. Xie, *IEEE Transactions on Applied Superconductivity* **29**, 1 (2019).
- [8] A. Vetter, S. Ferrari, P. Rath, R. Alaee, O. Kahl, V. Kovalyuk, S. Diewald, G. N. Goltsman, A. Korneev, C. Rockstuhl, *et al.*, *Nano Letters* **16**, 7085 (2016).
- [9] B. Korzh, Q. Zhao, S. Frasca, J. Allmaras, T. Autry, E. Bersin, M. Colangelo, G. Crouch, A. Dane, T. Gerrits, *et al.*, arXiv preprint arXiv:1804.06839 (2018).
- [10] I. E. Zadeh, J. W. Los, R. Gourgues, G. Bulgarini, S. M. Dobrovolskiy, V. Zwiller, and S. N. Dorenbos, arXiv preprint arXiv:1801.06574 (2018).
- [11] M. Caloz, B. Korzh, E. Ramirez, C. Schönerberger, R. J. Warburton, H. Zbinden, M. D. Shaw, and F. Bussiès, arXiv preprint arXiv:1906.02073 (2019).
- [12] C. Schuck, W. H. Pernice, and H. X. Tang, *Scientific Reports* **3**, 1893 (2013).
- [13] H. Shibata, K. Shimizu, H. Takesue, and Y. Tokura, *Optics Letters* **40**, 3428 (2015).
- [14] J. Sprengers, A. Gaggero, D. Sahin, S. Jahanmirinejad, G. Frucci, F. Mattioli, R. Leoni, J. Beetz, M. Lerner, M. Kamp, *et al.*, *Applied Physics Letters* **99**, 181110 (2011).
- [15] W. H. Pernice, C. Schuck, O. Minaeva, M. Li, G. Goltsman, A. Sergienko, and H. Tang, *Nature Communications* **3**, 1325 (2012).
- [16] C. Schuck, W. Pernice, and H. Tang, *Applied Physics Letters* **102**, 051101 (2013).
- [17] V. Kovalyuk, W. Hartmann, O. Kahl, N. Kaurova, A. Korneev, G. Goltsman, and W. Pernice, *Optics express* **21**, 22683 (2013).
- [18] D. Sahin, A. Gaggero, J.-W. Weber, I. Agafonov, M. A. Verheijen, F. Mattioli, J. Beetz, M. Kamp, S. Höfling, M. C. van de Sanden, *et al.*, *IEEE Journal of Selected Topics in Quantum Electronics* **21**, 1 (2015).
- [19] O. Kahl, S. Ferrari, V. Kovalyuk, G. N. Goltsman, A. Korneev, and W. H. Pernice, *Scientific reports* **5**, 10941 (2015).
- [20] P. Rath, O. Kahl, S. Ferrari, F. Sproll, G. Lewes-Malandrakis, D. Brink, K. Ilin, M. Siegel, C. Nebel, and W. Pernice, *Light: Science & Applications* **4**, e338 (2015).
- [21] F. Najafi, J. Mower, N. C. Harris, F. Bellei, A. Dane, C. Lee, X. Hu, P. Kharel, F. Marsili, S. Assefa, *et al.*, *Nature Communications* **6**, 5873 (2015).
- [22] J. Li, R. A. Kirkwood, L. J. Baker, D. Bosworth, K. Erotokritou, A. Banerjee, R. M. Heath, C. M. Natarajan, Z. H. Barber, M. Sorel, *et al.*, *Optics Express* **24**, 13931 (2016).
- [23] S. Ferrari, C. Schuck, and W. Pernice, *Nanophotonics* **7** (2018).
- [24] A. Gaggero, F. Martini, F. Mattioli, F. Chiarello, R. Cernansky, A. Politi, and R. Leoni, *Optica* **6**, 823 (2019).
- [25] H. Shibata, T. Hiraki, T. Tsuchizawa, K. Yamada, Y. Tokura, and S. Matsuo, *Superconductor Science and Technology* **32**, 034001 (2019).
- [26] A. Divochiy, F. Marsili, D. Bitauld, A. Gaggero, R. Leoni, F. Mattioli, A. Korneev, V. Seleznev, N. Kaurova, O. Minaeva, *et al.*, *Nature Photonics* **2**, 302 (2008).
- [27] R. Cheng, H. Yin, J. Liu, T. Li, H. Cai, Z. Xu, and W. Chen, *IEEE Transactions on Applied Superconductivity* **23**, 2200309 (2013).
- [28] D. Zhu, Q.-Y. Zhao, H. Choi, T.-J. Lu, A. E. Dane, D. Englund, and K. K. Berggren, *Nature Nanotechnology* , 1 (2018).
- [29] O. Kahl, S. Ferrari, V. Kovalyuk, A. Vetter, G. Lewes-Malandrakis, C. Nebel, A. Korneev, G. Goltsman, and W. Pernice, *Optica* **4**, 557 (2017).
- [30] R. Cheng, C.-L. Zou, X. Guo, S. Wang, X. Han, and H. X. Tang, *Nature communications* **10**, 1 (2019).
- [31] Y. Yun, A. Vetter, R. Stegmüller, S. Ferrari, W. H. Pernice, C. Rockstuhl, and C. Lee, arXiv preprint arXiv:1908.01681 (2019).
- [32] H. Takesue, S. W. Nam, Q. Zhang, R. H. Hadfield, T. Honjo, K. Tamaki, and Y. Yamamoto, *Nature photonics* **1**, 343 (2007).
- [33] S.-K. Liao, W.-Q. Cai, W.-Y. Liu, L. Zhang, Y. Li, J.-G. Ren, J. Yin, Q. Shen, Y. Cao, Z.-P. Li, *et al.*, *Nature* **549**, 43 (2017).
- [34] J. Wang, S. Paesani, Y. Ding, R. Santagati, P. Skrzypczyk, A. Salavrakos, J. Tura, R. Augusiak, L. Mančinska, D. Bacco, *et al.*, *Science* , eear7053 (2018).
- [35] D. Rosenberg, A. Kerman, R. Molnar, and E. Dauler, *Optics Express* **21**, 1440 (2013).
- [36] R. Cheng, X. Guo, X. Ma, L. Fan, K. Y. Fong, M. Poot, and H. X. Tang, *Optics Express* **24**, 27070 (2016).
- [37] R. Cheng, M. Poot, X. Guo, L. Fan, and H. X. Tang, *IEEE Transactions on Applied Superconductivity* **27**, 1 (2017).
- [38] S. Miki, M. Yabuno, T. Yamashita, and H. Terai, *Optics express* **25**, 6796 (2017).
- [39] B. Baek, A. E. Lita, V. Verma, and S. W. Nam, *Applied Physics Letters* **98**, 251105 (2011).
- [40] Y. P. Korneeva, M. Y. Mikhailov, Y. P. Pershin, N. Manova, A. Divochiy, Y. B. Vakhtomin, A. Korneev, K. Smirnov, A. Sivakov, A. Y. Devizenko, *et al.*, *Superconductor Science and Technology* **27**, 095012 (2014).
- [41] M. Caloz, M. Perrenoud, C. Autebert, B. Korzh, M. Weiss, C. Schönerberger, R. J. Warburton, H. Zbinden, and F. Bussiès, *Applied Physics Letters* **112**, 061103 (2018).
- [42] V. B. Verma, A. E. Lita, M. R. Vissers, F. Marsili, D. P. Pappas, R. P. Mirin, and S. W. Nam, *Applied Physics Letters* **105**, 022602 (2014).
- [43] J. P. Allmaras, A. Beyer, R. Briggs, F. Marsili, M. Shaw, G. Resta, J. Stern, V. Verma, R. Mirin, S. W. Nam, *et al.*, in *Lasers and Electro-Optics (CLEO), 2017 Conference on (IEEE,*

- 2017) pp. 1–2.
- [44] E. E. Wollman, V. B. Verma, A. E. Lita, W. H. Farr, M. D. Shaw, R. P. Mirin, and S. W. Nam, arXiv preprint arXiv:1908.10520 (2019).
- [45] V. B. Verma, B. Korzh, F. Bussieres, R. D. Horansky, A. E. Lita, F. Marsili, M. Shaw, H. Zbinden, R. Mirin, and S. Nam, *Applied Physics Letters* **105**, 122601 (2014).
- [46] F. Marsili, M. J. Stevens, A. Kozorezov, V. B. Verma, C. Lambert, J. A. Stern, R. D. Horansky, S. Dyer, S. Duff, D. P. Pappas, *et al.*, *Physical Review B* **93**, 094518 (2016).
- [47] S. Ferrari, V. Kovalyuk, W. Hartmann, A. Vetter, O. Kahl, C. Lee, A. Korneev, C. Rockstuhl, G. Gol'tsman, and W. Pernice, *Optics express* **25**, 8739 (2017).
- [48] L. Zhang, L. You, X. Yang, J. Wu, C. Lv, Q. Guo, W. Zhang, H. Li, W. Peng, Z. Wang, *et al.*, *Scientific reports* **8**, 1486 (2018).
- [49] M. J. Sowa, Y. Yemane, J. Zhang, J. C. Palmstrom, L. Ju, N. C. Strandwitz, F. B. Prinz, and J. Provine, *Journal of Vacuum Science & Technology A: Vacuum, Surfaces, and Films* **35**, 01B143 (2017).
- [50] O. Medeiros, M. Colangelo, I. Charaev, and K. K. Berggren, *Journal of Vacuum Science & Technology A: Vacuum, Surfaces, and Films* **37**, 041501 (2019).
- [51] F. Marsili, F. Najafi, E. Dauler, F. Bellei, X. Hu, M. Csete, R. J. Molnar, and K. K. Berggren, *Nano Letters* **11**, 2048 (2011).
- [52] E. Knehr, A. Kuzmin, M. Ziegler, S. Doerner, K. Ilin, M. Siegel, R. Stolz, and H. Schmidt, arXiv preprint arXiv:1906.05214 (2019).